

PAPER

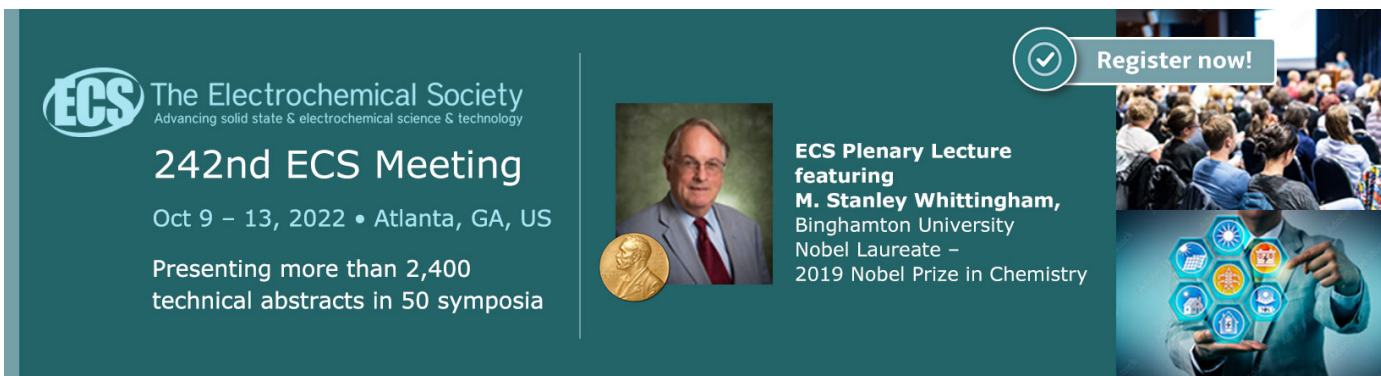
Study on time measurement for CSA-based readout electronics in STCF ECAL

To cite this article: L. Luo *et al* 2022 *JINST* **17** P02034

View the [article online](#) for updates and enhancements.

You may also like

- [The front-end data conversion and readout electronics for the CMS ECAL upgrade](#)
G. Mazza and S. Cometti
- [Search for light dark matter in the NA64 experiment](#)
S N Gninenko, N V Krasnikov and V A Matveev
- [Data filtering in the readout of the CMS Electromagnetic Calorimeter](#)
N Almeida, P Silva, J C Da Silva *et al.*





ECS The Electrochemical Society
Advancing solid state & electrochemical science & technology



242nd ECS Meeting

Oct 9 – 13, 2022 • Atlanta, GA, US

Presenting more than 2,400 technical abstracts in 50 symposia


ECS Plenary Lecture
featuring
M. Stanley Whittingham,
Binghamton University
Nobel Laureate –
2019 Nobel Prize in Chemistry

 Register now!



RECEIVED: September 21, 2021

REVISED: January 11, 2022

ACCEPTED: January 31, 2022

PUBLISHED: February 24, 2022

Study on time measurement for CSA-based readout electronics in STCF ECAL

L. Luo,^{a,b} Z. Jia,^{a,b} Z. Shen,^{a,b,*} Y. Zhang^{a,b} and S. Liu^{a,b}

^aState Key Laboratory of Particle Detection and Electronics, University of Science and Technology of China, Hefei 230026, China

^bDepartment of Modern Physics, University of Science and Technology of China, Hefei 230026, China

E-mail: henzt@ustc.edu.cn

ABSTRACT: Super Tau-Charm Facility (STCF) will provide unique support for particle physics research in China owing to its high luminosity and large dynamic range. Its electromagnetic calorimeter (ECAL) is designed as a new type of calorimeter which can perform high-precision energy and time measurement at the same time. Considering the high event rate and pile up induced by high luminosity, and the large channel number scale of ECAL, the readout electronics needs to adopt a high-precision, unconventional, and real-time processing method to reduce the data amount in transmission. Based on the charge-sensitive front-end electronics in energy measurement, an online time measurement method based on waveform fitting algorithm has been studied and implemented in this work. The parameters which would affect the time resolution are analyzed according to simulation and experimental test. After the optimization of electronics, a time resolution of 165 ps at the equivalent deposition energy of 1 GeV is achieved, which indicates that the waveform fitting method based on charge-sensitive readout electronics can meet the future requirements.

KEYWORDS: Front-end electronics for detector readout; Calorimeters

*Corresponding author.

Contents

1	Introduction	1
2	Time measurement method of waveform fitting based on CSA readout electronics	2
2.1	The electronics system and the algorithm of waveform fitting	2
2.2	Reconstruction of waveform template based on FFT	4
2.3	Simulation on the key parameters of waveform fitting method	6
2.4	Design and implementation of the waveform fitting algorithm in FPGA	7
2.5	Performance of waveform fitting algorithm based on CSA readout electronics	8
3	Discussion	11
3.1	The influence of system noise on the time resolution in waveform fitting method	11
3.2	Analysis of results before shaper and after shaper	12
3.3	Analysis of results at different sampling rates	13
4	Conclusion	15
A	Derive the fluctuations of the calculated results in waveform fitting algorithm	15
B	Improvement of time resolution with sequence selection optimization	17

1 Introduction

Super Tau-Charm Facility (STCF) will provide a unique platform for the research of tau-charm physics and hadron physics, which is one of the important options for accelerator-based particle physics after Beijing Electron-Positron Collider II (BEPC-II) in China [1, 2]. The electromagnetic calorimeter (ECAL), as an important part of the spectrometer, in addition to high-efficiency and high-precision gamma detection, also needs good enough time performance for background suppression and gamma-hadron discrimination, etc [2]. Due to the high background level induced by the high luminosity in STCF experiment, pure CsI is selected as the scintillation crystal owing to its fast response, high mass density and good radiation hardness [3, 4]. Considering the relatively low light yield of pure CsI crystal, the scintillation light is converted by avalanche photodiode (APD) to obtain an internal gain of 50.

The main purpose of STCF ECAL is to measure the energy of particles precisely, which are generated in the collision of electrons and positrons. In this respect, the readout system needs to process the photocurrent with sufficiently low noise in order to achieve good energy resolution. Hence, a front-end electronics system based on charge-sensitive amplifier (CSA) is developed and optimized to read out the signals from large area APD (LAAPD) which has a large junction capacitance of 270 pF [5].

In addition to the energy measurement, a good time resolution for STCF ECAL is also required in many applications, such as background suppression, gamma-neutron discrimination and identification of some interesting events. For example, on Spherical Neutral Detector (SND) deployed at the VEPP-2000 e^+e^- collider, a time resolution of about 1 ns is realized by fitting the shaped signal generated by NaI (Tl) and vacuum phototriode (VPT) [6]. The reconstructed time is used to identify the events with long EMC response time, e.g., $e^+e^- \rightarrow n\bar{n}$ (background events $e^+e^- \rightarrow p\bar{p}, \gamma\gamma$ near the threshold) [6]. In the future STCF experiment, to achieve gamma-neutron discrimination by time of flight, a time resolution better than 300 ps at 1 GeV is required for ECAL according to simulation.

However, the background in STCF can reach a level of several MHz due to the high luminosity, which would cause serious pileups. Traditional timing methods, like leading edge timing, are no longer suitable for these piled-up signals. In addition, due to the high event rate brought by the high luminosity and the scale of thousands of channels, the front-end electronics of ECAL also needs to have the ability to extract information online to reduce the pressure of data transmission and data storage. Hence, a real-time measurement method which can work well in high event rate needs to be studied and developed.

In section 2 of this paper, researches on a new timing method based on waveform fitting are detailed, including the readout electronics and algorithm adopted in this work, the reconstruction of waveform template based on fast Fourier transform (FFT), the simulation of some key parameters of the algorithm, the implementation of waveform fitting algorithm in Field-Programmable Gate Array (FPGA), and the results of experimental test. In section 3, some discussions are brought up, including the analysis of the results in simulation and experiment, the factors which would affect time resolution, and the optimization methods for better time performance.

2 Time measurement method of waveform fitting based on CSA readout electronics

The purpose of this work is to study a time measurement method on the basis of CSA readout circuit. In order to process the piled-up signals in the situation of high event rate, a waveform fitting method utilizing several sampling points is proposed and researched. In the following section, the details of the method are reported.

2.1 The electronics system and the algorithm of waveform fitting

The schematic layout and PCB pictures of the CSA electronics adopted in this work, which has been designed and optimized for charge measurement in STCF ECAL [5], are shown in figure 1. To avoid long-distance transmission, a separate system, which consists of Front End Board (FEB) and Back End Board (BEB), is employed. On FEB, the current signal is integrated by a CSA with JFET input stage which can reduce the electronics noise induced by the large input capacitance. Furthermore, a high bandwidth operational amplifier is adopted to achieve a sufficient close-loop bandwidth. On BEB, the pre-amplified signal can be firstly filtered by a $CR - RC^2$ shaper, or bypass the shaper. Then the signal is digitized by an Analog-to-Digital Convertor (ADC) and calculated in real time by the fitting algorithm embedded in FPGA. The fitting results are transmitted to the upper computer via Ethernet.

The waveform fitting algorithm is derived from the Belle II calorimeter upgrade electronics [7]. Sampling points are fitted by a template $F(t) = A \times f(t + \tau) + p$ by minimizing the chi square as

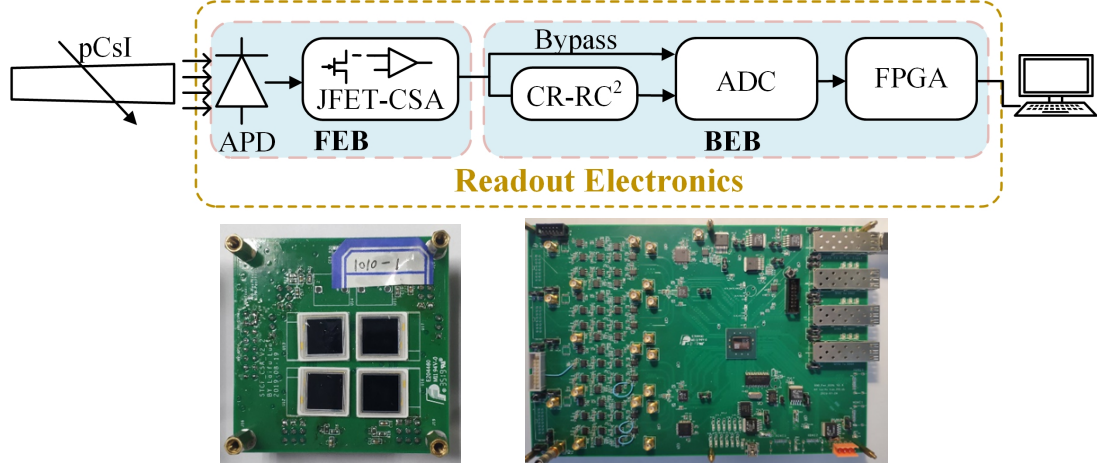


Figure 1. The schematic layout of the CSA electronics and PCB pictures.

shown in equation (2.1):

$$\chi^2 = \sum_{i,j} (y_i - A \cdot f(t_i + \tau) - p) \cdot S_{ij}^{-1} \cdot (y_j - A \cdot f(t_j + \tau) - p) \quad (2.1)$$

Where $f(t)$ is the template shape function, A is the signal amplitude to be measured, τ is the signal arrival time, p is the actual pedestal, y_i is the signal amplitude at t_i , $S_{ij} = \overline{(y_i - \bar{y}_i)(y_j - \bar{y}_j)}$ is the noise covariance matrix. Expand the template function to the first-order approximation, and the chi square can be changed into:

$$\chi^2 = \sum_{i,j} (y_i - Af(t_i) - A\tau f'(t_i) - p) \cdot S_{ij}^{-1} \cdot (y_j - Af(t_j) - A\tau f'(t_j) - p) \quad (2.2)$$

Tabulate the template function $f(t)$ and its derivative $f'(t)$ to obtain the table of \mathbf{f} and \mathbf{f}' . $f_{ki} = f(t_{ki}) = f(k\delta t + i\Delta t)$, where Δt is the sampling period of ADC and δt is the bin width of tabulation, i and k are the corresponding bin index. Replace the relevant items in equation (2.2) with tabular data:

$$\chi^2 = \sum_{i,j} (y_i - Af_{ki} - Bf'_{ki} - p) \cdot S_{ij}^{-1} \cdot (y_j - Af_{kj} - Bf'_{kj} - p) \quad (2.3)$$

Where $B = A\tau$. Expand equation (2.3) by the condition that the partial derivative is zero and the inverse noise covariance matrix is symmetrical:

$$\begin{cases} \sum_{i,j} f_{ki} \cdot S_{ij}^{-1} \cdot (y_j - Af_{kj} - Bf'_{kj} - p) = 0 \\ \sum_{i,j} f'_{ki} \cdot S_{ij}^{-1} \cdot (y_j - Af_{kj} - Bf'_{kj} - p) = 0 \\ \sum_{i,j} 1 \cdot S_{ij}^{-1} \cdot (y_j - Af_{kj} - Bf'_{kj} - p) = 0 \end{cases} \quad (2.4)$$

Rewrite it into matrix form and the results can be expressed as equation (2.5). The time information

can be extracted according to $\tau = B/A$.

$$\begin{aligned} & \begin{pmatrix} \mathbf{f}_k^T \cdot \mathbf{S}^{-1} \cdot \mathbf{f}_k & \mathbf{f}_k^T \cdot \mathbf{S}^{-1} \cdot \mathbf{f}'_k & \mathbf{f}_k^T \cdot \mathbf{S}^{-1} \cdot \mathbf{I} \\ \mathbf{f}'_k{}^T \cdot \mathbf{S}^{-1} \cdot \mathbf{f}_k & \mathbf{f}'_k{}^T \cdot \mathbf{S}^{-1} \cdot \mathbf{f}'_k & \mathbf{f}'_k{}^T \cdot \mathbf{S}^{-1} \cdot \mathbf{I} \\ \mathbf{I}^T \cdot \mathbf{S}^{-1} \cdot \mathbf{f}_k & \mathbf{I}^T \cdot \mathbf{S}^{-1} \cdot \mathbf{f}'_k & \mathbf{I}^T \cdot \mathbf{S}^{-1} \cdot \mathbf{I} \end{pmatrix} \cdot \begin{pmatrix} A \\ B \\ p \end{pmatrix} = \begin{pmatrix} \mathbf{f}_k^T \cdot \mathbf{S}^{-1} \cdot \mathbf{Y} \\ \mathbf{f}'_k{}^T \cdot \mathbf{S}^{-1} \cdot \mathbf{Y} \\ \mathbf{I}^T \cdot \mathbf{S}^{-1} \cdot \mathbf{Y} \end{pmatrix} \\ & \begin{pmatrix} A \\ B \\ p \end{pmatrix} = \begin{pmatrix} \mathbf{f}_k^T \cdot \mathbf{S}^{-1} \cdot \mathbf{f}_k & \mathbf{f}_k^T \cdot \mathbf{S}^{-1} \cdot \mathbf{f}'_k & \mathbf{f}_k^T \cdot \mathbf{S}^{-1} \cdot \mathbf{I} \\ \mathbf{f}'_k{}^T \cdot \mathbf{S}^{-1} \cdot \mathbf{f}_k & \mathbf{f}'_k{}^T \cdot \mathbf{S}^{-1} \cdot \mathbf{f}'_k & \mathbf{f}'_k{}^T \cdot \mathbf{S}^{-1} \cdot \mathbf{I} \\ \mathbf{I}^T \cdot \mathbf{S}^{-1} \cdot \mathbf{f}_k & \mathbf{I}^T \cdot \mathbf{S}^{-1} \cdot \mathbf{f}'_k & \mathbf{I}^T \cdot \mathbf{S}^{-1} \cdot \mathbf{I} \end{pmatrix}^{-1} \cdot \begin{pmatrix} \mathbf{f}_k^T \cdot \mathbf{S}^{-1} \cdot \mathbf{Y} \\ \mathbf{f}'_k{}^T \cdot \mathbf{S}^{-1} \cdot \mathbf{Y} \\ \mathbf{I}^T \cdot \mathbf{S}^{-1} \cdot \mathbf{Y} \end{pmatrix} \end{aligned} \quad (2.5)$$

In the actual algorithm, the vector \mathbf{Y} used for fitting is a sequence around the peak of the waveform. The expanded form of \mathbf{Y} is $(y_1, y_2, \dots, y_{n-1}, y_n)^T$. The noise covariance matrix is a n-order symmetrical square matrix and the expanded form is:

$$\begin{pmatrix} S_{1,1} & \cdots & S_{1,n} \\ \vdots & \ddots & \vdots \\ S_{n,1} & \cdots & S_{n,n} \end{pmatrix}$$

The template tabulation \mathbf{f} is a matrix in which the row represents one sampling sequence and the column represents the waveform amplitudes at several consecutive phases in one cycle. The derivative tabulation \mathbf{f}' has the same order and form as \mathbf{f} . In the calculation of equation (2.5), \mathbf{f}_k represents a row vector of length n taken from the template matrix starting from a certain element. For example, in the first iteration, $\mathbf{f}_1 = (f_{1,1}, f_{1,2}, \dots, f_{1,n-1}, f_{1,n})^T$ represents a sequence starting from the first phase of the first sampling point. In the m -th iteration, $\mathbf{f}_m = (f_{\alpha_m, \beta_m}, f_{\alpha_m, \beta_m+1}, \dots, f_{\alpha_m, \beta_m+n-2}, f_{\alpha_m, \beta_m+n-1})^T$, where α_m and β_m are calculated from the previous iteration result according to equation (2.6):

$$\begin{aligned} \alpha_m &= \alpha_{m-1} + \Delta\alpha, \quad \beta_m = \beta_{m-1} + \Delta\beta \\ \Delta\alpha \cdot \delta t + \Delta\beta \cdot \Delta t &= \tau_{m-1} = \frac{B_{m-1}}{A_{m-1}} \end{aligned} \quad (2.6)$$

After several iterations, the calculated time τ_m converge to a value which is smaller than the bin width of the template tabulation (δt). Hence, the position parameter α and β have also converged and the signal arrival time τ can be obtained:

$$\tau = \sum \tau_i = (\alpha - 1) \cdot \delta t + (\beta - 1) \cdot \Delta t \quad (2.7)$$

2.2 Reconstruction of waveform template based on FFT

The previous description indicates that the accuracy of waveform template tabulation (δt) directly affects the time resolution of the readout system. To obtain an accurate template, one reconstruction algorithm based on FFT is proposed in this work. Due to the randomness between the arrival time of the signal and the rising edge of the sampling clock, as shown in figure 2, the interval τ between the peak point of the pre-amplified signal and the rising edge of the sampling clock, obeys a uniform distribution from 0 to T (period of ADC clock).

According to the corresponding relationship between time domain and frequency domain, the phase difference after FFT has a linear correlation with the time shift. Assume the phase difference and time shift in figure 2 are related to each other by a proportional coefficient k at one certain frequency:

$$\Delta\varphi = k\tau, \quad \varphi_i = k\tau_i + \varphi_0 \quad (2.8)$$

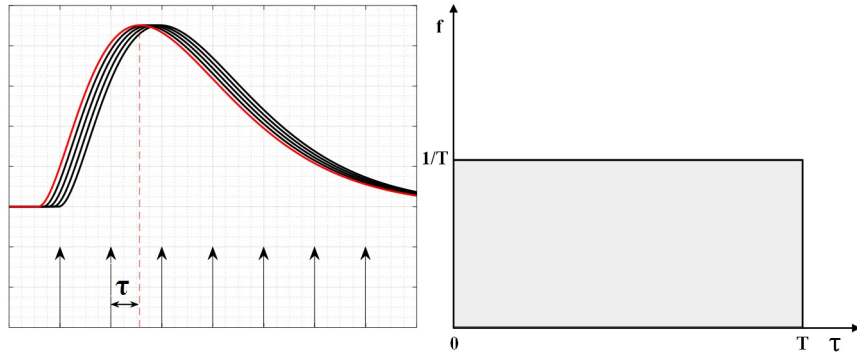


Figure 2. The relative position distribution of signals from FEB in one ADC cycle.

Where φ_0 is the phase of the waveform whose peak is just at the rising edge of sampling clock. The sequence τ_i obeys the uniform distribution in the interval from 0 to T , so the corresponding sequence φ_i also obeys a uniform distribution in another certain interval. According to the nature of variance, the proportional coefficient k can be calculated by equation (2.9):

$$k = \sqrt{\frac{\text{Var}(\varphi)}{\text{Var}(\tau)}} = \sqrt{\frac{\text{Var}(\varphi)}{T^2/12}} = \frac{2\sqrt{3} \text{Var}(\varphi)}{T} \quad (2.9)$$

On the basis of k , all phases can be transformed to the average phase by addition or subtraction. That means the waveform can be shift to a certain position where the peak is right in the middle of the sampling clock. The shift time can be obtained according to equation (2.10):

$$t_i = \tau_i - \tau_{\text{middle}} = \frac{\varphi_i - \overline{\varphi_i}}{k} \quad (2.10)$$

Hence, the sampling waveform sequence (nT, y_n) is changed into $(nT - t_i, y_n)$, where n represents the n -th sampling point. The algorithm effect of processing two sampling sequences is shown in figure 3.

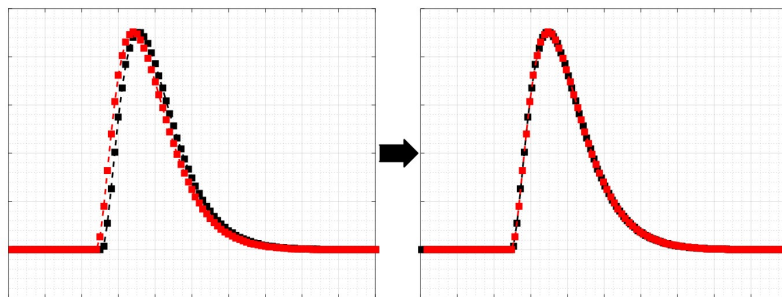


Figure 3. The effect of reconstruction algorithm processing two sample sequences.

As a result, a waveform tabulation with much higher precision can be obtained after processing multiple sequences. In the actual waveform reconstruction, 10000 waveforms are utilized to reconstruct a template tabulation with a time accuracy of 10 ps.

2.3 Simulation on the key parameters of waveform fitting method

Before designing and implementing the waveform fitting algorithm in FPGA, some key parameters need to be simulated and verified.

In the aspect of charge measurement, the signal from FEB is filtered by a $CR-RC^2$ shaper and then digitized by an ADC to ensure good signal-to-noise ratio [5]. In the time measurement, whether the shaped signal is suitable and capable for waveform fitting needs to be confirmed. Therefore, a simulation in MATLAB is carried out to compare the timing performance of the unfiltered and filtered signals, which are before and after shaper respectively. The simulation flow chart is shown in figure 4. The waveform input for simulation is the combination of the shape function derived from actual signals and the noise generated in MATLAB. The noise waveform adopted in simulation is obtained from the APD noise power density spectrum in theoretical model [5] passing through different transfer functions. In the simulation process, one input signal is directly sampled to generate a waveform sequence recorded as “channel 1”. The other signal is firstly delayed for a fixed time and then sampled to get the other sequence recorded as “channel 2”. The two sequences are superimposed with two noise sequences, and then calculated by the waveform fitting algorithm respectively. The fixed interval between two channels can be extracted according to the fitting results.

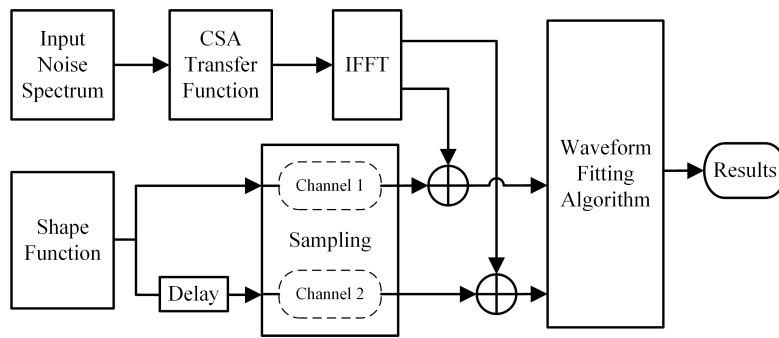


Figure 4. The flow chart of simulation in MATLAB.

The simulation results of the waveform fitting algorithm with unfiltered and filtered signals at different amplitude are shown in figure 5. The fitting algorithm can realize a time resolution of 153 ps and 475 ps with signals before shaper and after shaper respectively, at the input charge of 200 fC (equivalent deposition energy of 1 GeV). Assuming that the crystal luminescence and the readout electronics have the same and independent contribution on the time resolution of ECAL, it means that the timing accuracy of readout electronics needs to be better than 212 ps. As a result, waveform fitting with sampling points after shaper cannot meet the demand.

After it is clear that the unfiltered signals before shaper are necessary for fitting algorithm, another important parameter of sampling frequency has also been simulated. In the flow chart of figure 4, different sampling frequencies of 50 MSPS, 100 MSPS and 125 MSPS are employed to compare the fitting performance. The simulation results are shown in figure 6. Increasing the sampling rate from 50 MSPS to 125 MSPS, the time resolution of waveform fitting can be reduced from 184 ps to 151 ps (153 ps at 100 MSPS).

In summary, compared with signals after shaper, unfiltered signals before shaper can achieve better timing accuracy. Moreover, increasing the sampling frequency of ADC can improve the time

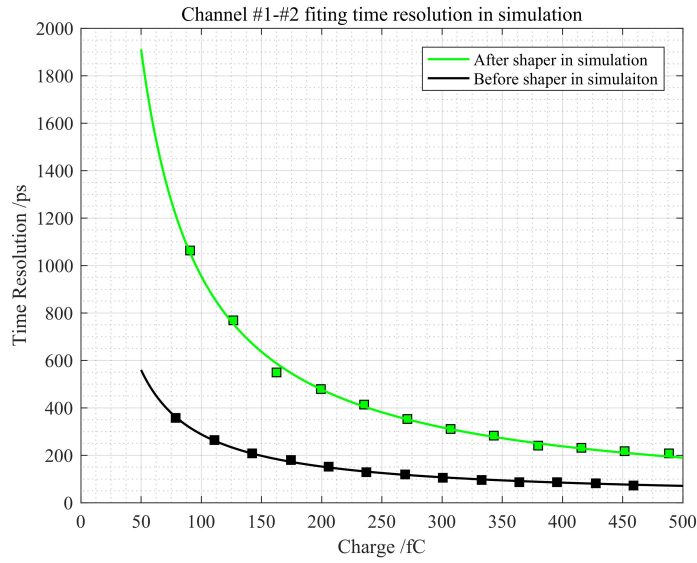


Figure 5. Simulation results of the algorithm utilizing signals before and after shaper.

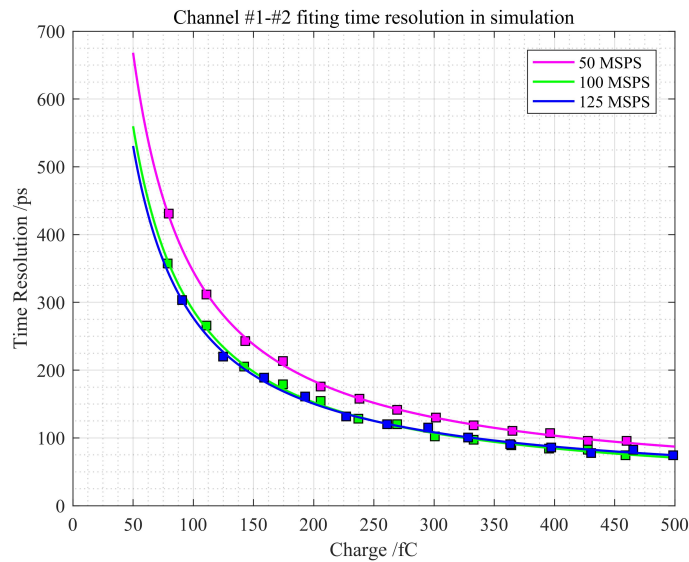


Figure 6. Simulation results of the algorithm utilizing unfiltered signals at different sampling frequencies.

resolution of waveform fitting method. However, the improvement from 100 MSPS to 125 MSPS is not obvious, and it needs to be verified in experiments.

2.4 Design and implementation of the waveform fitting algorithm in FPGA

Due to the high luminosity of STCF experiment, the event rate of ECAL is expected to reach several MHz. If the waveforms of thousands of channels are all transmitted to the back-end server for calculation, it will cause great transmission pressure and storage waste. Therefore, it is beneficial and necessary to extract information in real time at the front end.

Hence, after the simulation on the key parameters of waveform fitting, design and implementation of this algorithm in FPGA have been carried out. The block diagram of the fitting algorithm embedded in FPGA is shown in figure 7. The algorithm mainly consists of two modules, “Waveform Fitting Matrix Calculation Module (WFMCM)” and “Iteration Control Module”.

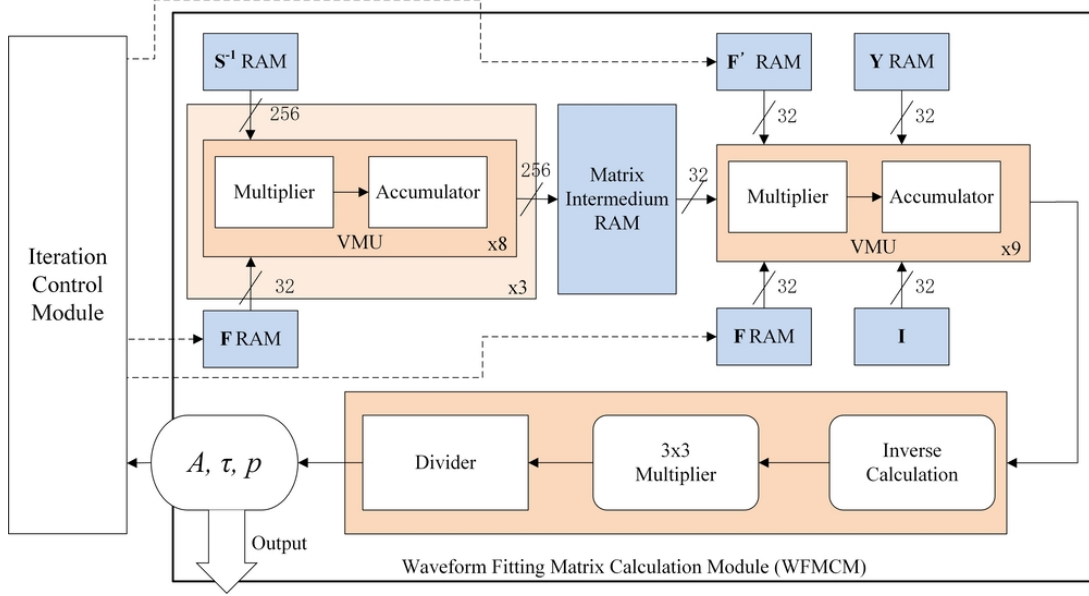


Figure 7. The module of waveform fitting algorithm embedded in FPGA.

In the WFMCM, the calculation of each matrix element is divided into two sub-processes. For example, the calculation of $\mathbf{f}_k \cdot \mathbf{S}^{-1} \cdot \mathbf{f}_k^T$ in equation (2.5) is divided into $\mathbf{Tmp} = \mathbf{f}_k \cdot \mathbf{S}^{-1}$ and $\mathbf{Tmp} \cdot \mathbf{f}_k^T$. Each sub-process is completed by several vector multiplication units (VMU), and every VMU is composed of a floating-point multiplier and a floating-point accumulator. One VMU can complete the multiplication process of two n -th order vectors in n cycles. The input data for multiplication is read from block RAMs in FPGA. With the calculated results of matrix element, the fitting parameters of A , B (which equals to $A\tau$), and p can be obtained after a few subsequent calculations, i.e., third-order matrix inverse operation, multiplication and division.

As shown in equation (2.6) and equation (2.7), the relative phase of the waveform to the template needs to be calculated iteratively until the i -th result τ_i is smaller than the template tabulation accuracy (δt). After some experimental verifications, 3 to 4 iterations can make the result τ_i smaller than δt . Hence, 5 iterations which are slightly larger than experimental result are selected in the FPGA algorithm.

After Iterative calculation of WFMCM, the waveform fitting results are converged. Then the converged results are output and uploaded to the data acquisition computer. All of the online fitting modules are running in the 160 MHz clock domain, and the resource utilization of FPGA adopted in this work (XC7k160T from Xilinx) is summarized in table 1.

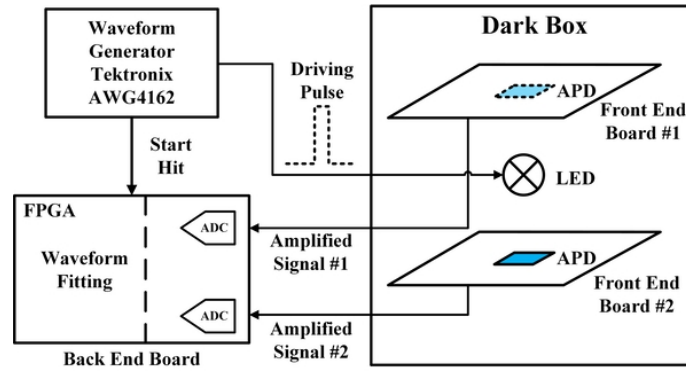
2.5 Performance of waveform fitting algorithm based on CSA readout electronics

After the implementation of the algorithm in FPGA, some experimental tests have been carried out to examine the timing accuracy of waveform fitting based on the CSA readout electronics. The

Table 1. FPGA resource utilization in different fitting algorithms.

Resources	Utilization (before shaper, $n = 8$)	Utilization (After shaper, $n = 32$)
LUT	27741 (27.36%)	62731 (61.86%)
FF	28820 (14.21%)	66368 (32.73%)
BRAM	128.5 (39.54%)	262.5 (80.77%)
DSP	159 (26.5%)	375 (62.5%)

experimental diagram is shown in figure 8. Like simulations in section 2.3, the measuring accuracy of the inherent delay between two FEBs is selected to reflect the performance of this algorithm. As shown in the diagram, an LED is driven by a pulse generated by Tektronix Arbitrary Waveform Generator AWG4162, which has a rising and falling edge of 800 ps, a width of 10 ns and a frequency of 100 kHz. The APDs on two FEBs receive the LED light and convert it into current signals. The two current signals are integrated by two CSAs respectively, and transmitted to a same BEB for digitizing. The digital data of two FEBs are then calculated by the fitting algorithm in FPGA. In addition, the Start Hit in the diagram is only used as a flag to start sampling.

**Figure 8.** The block diagram of experiment for waveform fitting.

The first test is to verify the timing performance of this algorithm processing unfiltered signals and filtered signals, which are before shaper and after shaper respectively. According to the results shown in figure 9, the waveform fitting method realizes a time resolution of 169 ps and 464 ps respectively, which are consistent with the simulation results. As a result, sampling points after shaper are not suitable for fitting algorithm and the waveform sequences before shaper need to be adopted in waveform fitting.

Another experiment is to test the timing performance of the waveform fitting algorithm dealing with the signals at different sampling rates. The test diagram is the same as the one shown in figure 8. The clock frequency of ADC on BEB is changed from 50 MSPS to 125 MSPS, and the test results are shown in figure 10. According to the test results, the waveform fitting algorithm achieves a time resolution of 219 ps, 169 ps and 165 ps at the sampling frequency of 50 MSPS, 100 MSPS and 125 MSPS respectively. The time resolution improves with higher sampling rates, which is consistent with the simulation results. But the improvement from 100 MSPS to 125 MSPS is not obvious, same as the trend in simulation. On the other hand, the timing results in experiment are worse than the

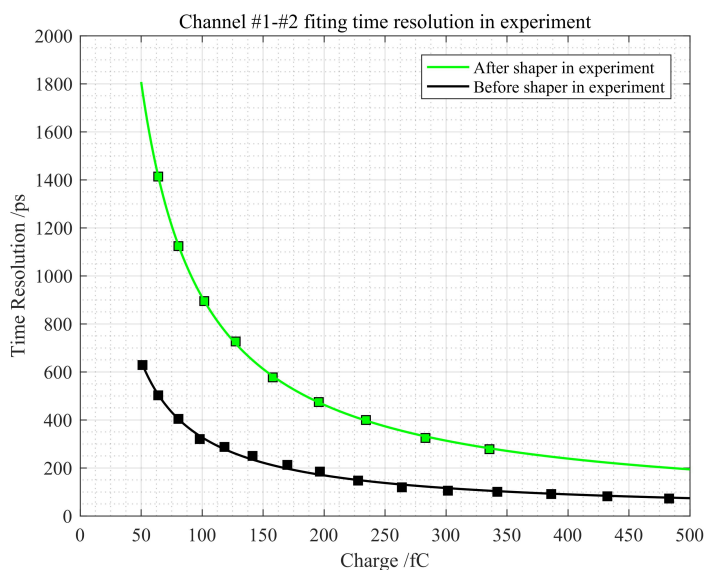


Figure 9. Time resolution of waveform fitting algorithm utilizing signals before and after shaper in experiment.

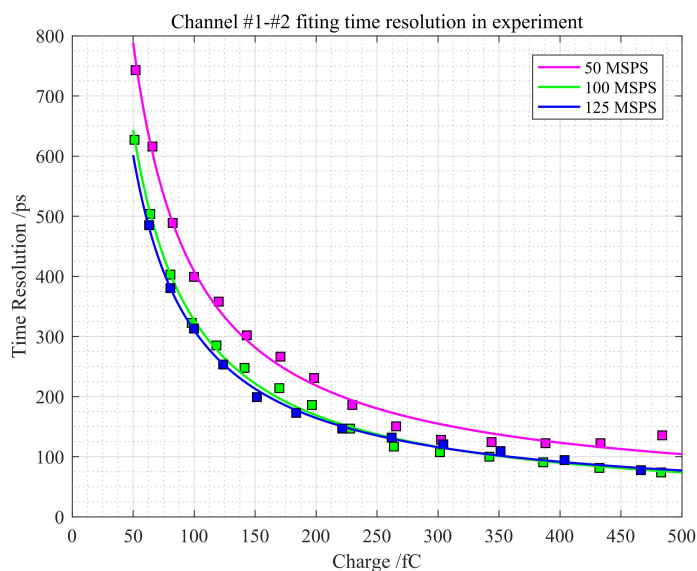


Figure 10. Time resolution of waveform fitting algorithm processing signals before shaper at different sampling frequencies.

ones in simulation, which might be caused by the slight difference between experimental waveforms and template. The resolution of 219 ps in experiment is beyond the theoretical requirement, so 50 MSPS cannot be used in subsequent works.

In summary, owing to the steeper edges of unfiltered signals, the fitting algorithm can realize a better time resolution with signals before shaper. In the aspect of sampling rate, the timing accuracy gets better as the sampling frequency increases. The results at 100 MSPS and 125 MSPS which have no obvious difference both meet the preliminary requirement.

3 Discussion

3.1 The influence of system noise on the time resolution in waveform fitting method

In the previous experimental results, the time resolution is inversely proportional to the amount of input charge. This is mainly caused by the system noise at sampling points. On the basis of equation (2.3), add an infinitesimal \tilde{A} , \tilde{B} , \tilde{p} of the three parameters A , B , p to the chi-square which has been minimized, and equation (3.1) can be obtained:

$$\chi^2 = \sum_{i,j} (no_i - \tilde{A}f_{ki} - \tilde{B}f'_{ki} - \tilde{p}) \cdot S_{ij}^{-1} \cdot (no_j - \tilde{A}f_{kj} - \tilde{B}f'_{kj} - \tilde{p}) \quad (3.1)$$

Where $no_i = y_i - Af_{ki} - Bf'_{ki} - p$ represents the noise at the i -th sampling point when the parameters of A , B , p are the values which minimize the chi-square. Equation (3.1) represents the correlation between system noise and the fluctuation of the parameters to be measured. Applying the condition that the partial derivative is zero, the correlation between the infinitesimals and the system noise can be expressed as equation (3.2), which has a similar form to equation (2.5):

$$\begin{pmatrix} \mathbf{f}_k^T \cdot \mathbf{S}^{-1} \cdot \mathbf{f}_k & \mathbf{f}_k^T \cdot \mathbf{S}^{-1} \cdot \mathbf{f}'_k & \mathbf{f}_k^T \cdot \mathbf{S}^{-1} \cdot \mathbf{I} \\ \mathbf{f}'_k{}^T \cdot \mathbf{S}^{-1} \cdot \mathbf{f}_k & \mathbf{f}'_k{}^T \cdot \mathbf{S}^{-1} \cdot \mathbf{f}'_k & \mathbf{f}'_k{}^T \cdot \mathbf{S}^{-1} \cdot \mathbf{I} \\ \mathbf{I}^T \cdot \mathbf{S}^{-1} \cdot \mathbf{f}_k & \mathbf{I}^T \cdot \mathbf{S}^{-1} \cdot \mathbf{f}'_k & \mathbf{I}^T \cdot \mathbf{S}^{-1} \cdot \mathbf{I} \end{pmatrix} \cdot \begin{pmatrix} \tilde{A} \\ \tilde{B} \\ \tilde{p} \end{pmatrix} = \begin{pmatrix} \mathbf{f}_k^T \cdot \mathbf{S}^{-1} \cdot \mathbf{N} \\ \mathbf{f}'_k{}^T \cdot \mathbf{S}^{-1} \cdot \mathbf{N} \\ \mathbf{I}^T \cdot \mathbf{S}^{-1} \cdot \mathbf{N} \end{pmatrix} \quad (3.2)$$

$$\begin{pmatrix} \tilde{A} \\ \tilde{B} \\ \tilde{p} \end{pmatrix} = \begin{pmatrix} \mathbf{f}_k^T \cdot \mathbf{S}^{-1} \cdot \mathbf{f}_k & \mathbf{f}_k^T \cdot \mathbf{S}^{-1} \cdot \mathbf{f}'_k & \mathbf{f}_k^T \cdot \mathbf{S}^{-1} \cdot \mathbf{I} \\ \mathbf{f}'_k{}^T \cdot \mathbf{S}^{-1} \cdot \mathbf{f}_k & \mathbf{f}'_k{}^T \cdot \mathbf{S}^{-1} \cdot \mathbf{f}'_k & \mathbf{f}'_k{}^T \cdot \mathbf{S}^{-1} \cdot \mathbf{I} \\ \mathbf{I}^T \cdot \mathbf{S}^{-1} \cdot \mathbf{f}_k & \mathbf{I}^T \cdot \mathbf{S}^{-1} \cdot \mathbf{f}'_k & \mathbf{I}^T \cdot \mathbf{S}^{-1} \cdot \mathbf{I} \end{pmatrix}^{-1} \cdot \begin{pmatrix} \mathbf{f}_k^T \cdot \mathbf{S}^{-1} \cdot \mathbf{N} \\ \mathbf{f}'_k{}^T \cdot \mathbf{S}^{-1} \cdot \mathbf{N} \\ \mathbf{I}^T \cdot \mathbf{S}^{-1} \cdot \mathbf{N} \end{pmatrix}$$

Where $\mathbf{N} = (no_1, no_2, \dots, no_n)^T$ represents the noise at the sampling points. Rewrite it into matrix form:

$$\tilde{\boldsymbol{\beta}} = (\mathbf{X}^T \mathbf{S}^{-1} \mathbf{X})^{-1} \mathbf{X}^T \mathbf{S}^{-1} \mathbf{N} \quad (3.3)$$

Where \mathbf{X} is the matrix of template information and $\tilde{\boldsymbol{\beta}}$ is the error of three parameters induced by noise. Their expanded forms are expressed as below:

$$\tilde{\boldsymbol{\beta}} = \begin{pmatrix} \tilde{A} \\ \tilde{B} \\ \tilde{p} \end{pmatrix}, \quad \mathbf{X} = \begin{pmatrix} f_{k,1} & f'_{k,1} & 1 \\ \vdots & \vdots & \vdots \\ f_{k,n} & f'_{k,n} & 1 \end{pmatrix} \quad (3.4)$$

The variance of $\tilde{\boldsymbol{\beta}}$ and its element can be calculated and shown in equation (3.5):

$$\begin{aligned} \text{Var}(\tilde{\boldsymbol{\beta}}) &= E[(\tilde{\boldsymbol{\beta}} - E[\tilde{\boldsymbol{\beta}}])(\tilde{\boldsymbol{\beta}} - E[\tilde{\boldsymbol{\beta}}])^T] = (\mathbf{X}^T \mathbf{S}^{-1} \mathbf{X})^{-1} \\ \text{Var}(\tilde{\beta}_i) &= ((\mathbf{X}^T \mathbf{S}^{-1} \mathbf{X})^{-1})_{ii} \end{aligned} \quad (3.5)$$

The detailed derivation process can be found in the appendix A. Hence, the time jitter induced by system noise at sampling points is:

$$\text{Var}(\tilde{\tau}) = \frac{1}{A^2} ((\mathbf{X}^T \mathbf{S}^{-1} \mathbf{X})^{-1})_{22}, \quad \sigma_{t-n} = \frac{1}{A} \sqrt{((\mathbf{X}^T \mathbf{S}^{-1} \mathbf{X})^{-1})_{22}} \quad (3.6)$$

From equation (3.6), it can be conducted that the noise-induced jitter has an inverse proportional relationship with the signal amplitude A which is proportional to the amount of input charge. On the other hand, matrix \mathbf{X} with larger derivative for waveform fitting can reduce the influence of system noise on the time resolution.

3.2 Analysis of results before shaper and after shaper

In the previous results of waveform fitting algorithm processing unfiltered and filtered signals before and after shaper, the time resolution in experiment is consistent with the one in simulation. Furthermore, the timing accuracy of filtered signals is about 300 ps worse than the one of unfiltered. Based on the theoretical study of the noise effect on timing accuracy in section 3.1, the source which causes the difference in time resolution before and after shaper is analyzed below.

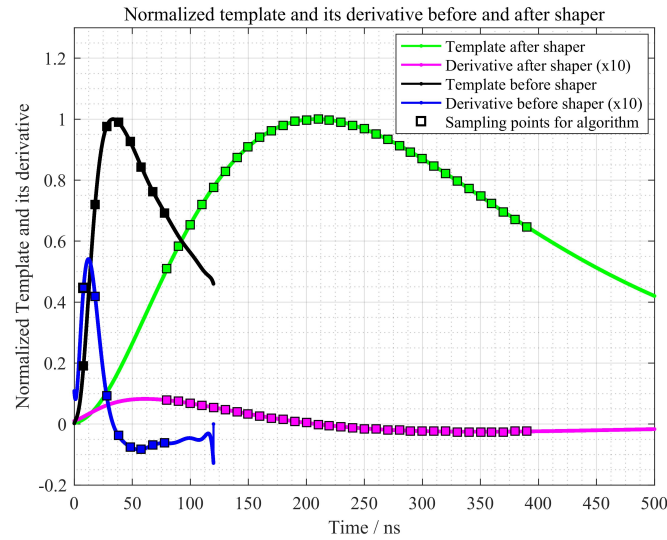


Figure 11. The normalized template and its derivative before shaper and after shaper.

As shown in figure 11, the peaking time of template after shaper is about 200 ns while the one before shaper is less than 40 ns. As a result, the derivative after shaper is much smaller compared with the other one (the amplitude of derivative is magnified 10 times because it is too small compared to the template). The squares in figure 11 represent the position of the sampling points in the template. Based on the values of template and derivative at squares, the time jitter induced by noise can be calculated according to equation (3.6). Since the jitter calculation requires the information of all sampling points, the first point is selected to represent one sequence when studying the correlation between timing accuracy and sampling sequences. Figure 12 (a) shows the time distribution of the first point in the sequence used for fitting algorithm. The first point of sequence before shaper is distributed between 10 ns and 20 ns in template, while the one after shaper is from 85 ns to 95 ns. According to the results of noise induced timing accuracy under different sampling sequences in figure 12 (b), the value range of the timing fluctuation in experiment is limited to the green box and the gray box. The final time resolution is the average result within each box. On this basis, the calculated average time resolution at different input charge is displayed in figure 13, which is in good agreement with the experimental results.

In summary, the bad time resolution of filtered signals after shaper in experiment is mainly caused by the noise and the slow waveform shape. Besides, it can be conducted from figure 12 that optimizing the selection of fitting sequence can reduce the noise influence. The detail improvement by choosing sequence whose first point is close to 0 ns is added in the appendix B. However, signals

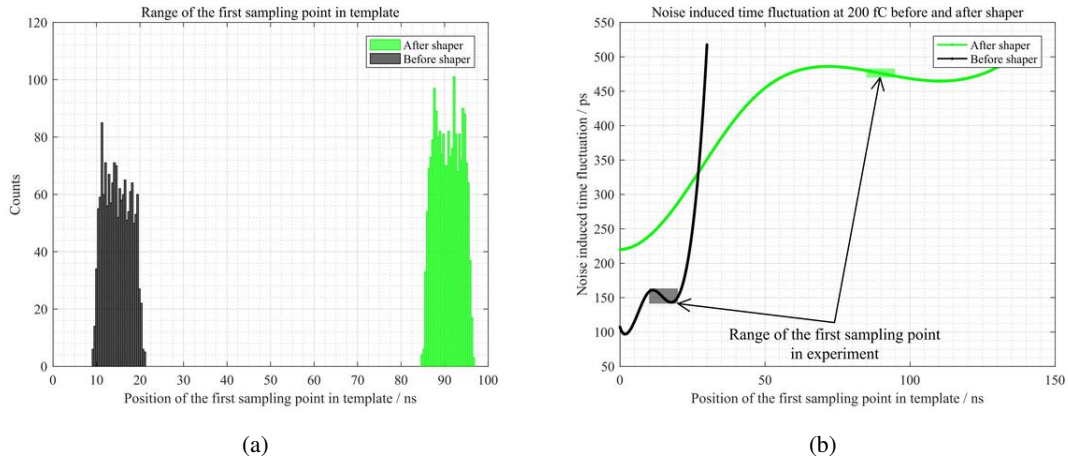


Figure 12. (a): The time distribution of the first point before and after shaper in the experiment. (b): The noise induced jitter with different fitting sequences (the horizontal axis represents the time of the first point).

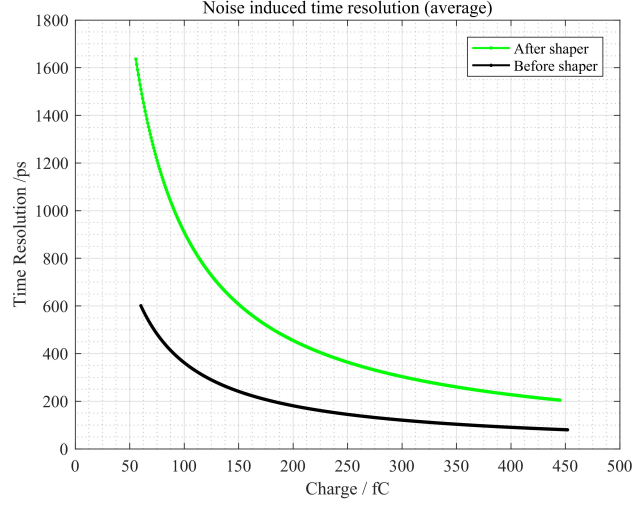


Figure 13. The average noise induced time resolution based on calculation at different input charge.

after shaper still cannot meet demand of the future experiment and unfiltered signals are necessary for this fitting algorithm.

3.3 Analysis of results at different sampling rates

Another important parameter in the waveform fitting algorithm is the sampling rate. In the previous simulation and experiment, the time resolution improves as the sampling rate increases. Furthermore, the time resolution gets a reduction of tens of picoseconds when the sampling rate increases from 50 MSPS to 100 MSPS. However, it changes only a few picoseconds when the sampling rate rises from 100 MSPS to 125 MSPS. These phenomena will be discussed below.

Same as the analysis of time resolution before and after shaper in section 3.2, extract the time distribution of the first point in the sequence at different sampling rate. The detail is shown in

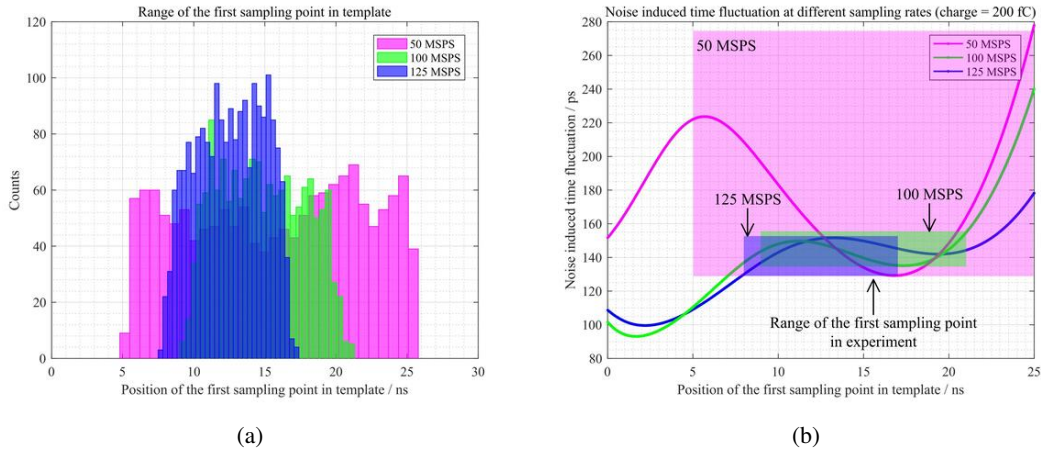


Figure 14. (a): The time distribution of the first point at different sampling rates in the experiment. (b): The noise induced jitter with different fitting sequences (the horizontal axis represents the time of the first point).

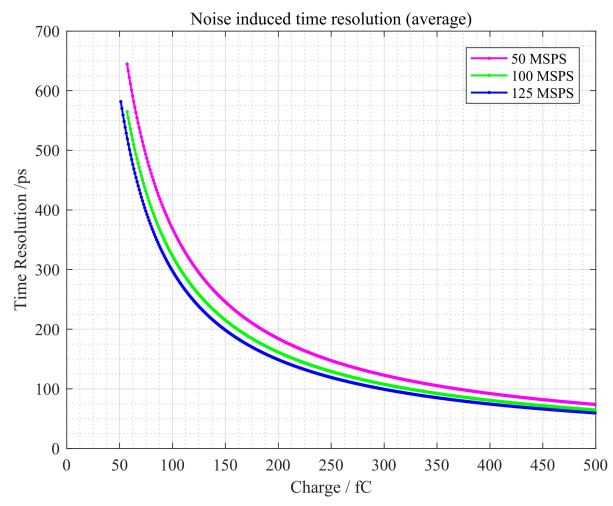


Figure 15. The relationship between the average noise induced time resolution based on calculation and the input charge at different sampling rates.

figure 14 (a). The first point of sequence used for calculation varies from 5 ns to 25 ns at 50 MSPS, 9 ns to 21 ns at 100 MSPS and 8 ns to 17 ns at 125 MSPS. At the same time, the relationship between the noise induced timing fluctuation and the sequence at different sampling rates can be calculated according to equation (3.6). The curves in figure 14 (b) are the calculated results. Hence, the range of the timing fluctuation at different sampling rates can be figured out, as shown in the three boxes. It can be clearly seen that the timing fluctuation range at 50 MSPS is much larger than the other two results. Besides, the fluctuation range at 100 MSPS is very close to the one at 125 MSPS, because the two relationship curves are close to each other. Therefore, in terms of the average result, the resolution of 50 MSPS will be much worse than that of 100 MSPS and 125 MSPS, while there is no big difference between the latter two results. The calculated average time resolution at different input charge is shown in figure 15, which is consistent with the results in simulation and in experiment.

In summary, the timing fluctuation of waveform fitting method is mainly caused by the noise at every sampling point. Signals after shaper cannot satisfy the requirement due to its small derivative, so it is necessary to adopt unfiltered signals in this algorithm. In addition, the time resolution improves as the sampling rate increases. However, the increase of sampling rate has less contribution to the time resolution when it is higher than 100 MSPS. Therefore, both 100 MSPS and 125 MSPS can be applied as the sampling rate in subsequent work. For future STCF experiments, the specific influence of crystal luminescence needs to be verified, in order to provide a basis for the final selection of sampling rate.

4 Conclusion

STCF can provide support for particle physics research in tau-charm energy region owing to its high luminosity. As one of the important detectors, ECAL not only needs high energy resolution in gamma detection, but also need excellent time resolution to achieve background suppression, gamma-neutron discrimination, etc. In this paper, a time measurement method of waveform fitting based on the CSA readout electronics is studied and implemented. On the basis of simulation and experimental test, the parameters which would affect the time resolution are analyzed. After optimization of the readout system, a time resolution of 165 ps with unfiltered signals at 125 MSPS sampling frequency is achieved. The experimental result indicates that the waveform fitting method based on CSA readout electronics satisfies the requirement.

A Derive the fluctuations of the calculated results in waveform fitting algorithm

In waveform fitting algorithm, all of the waveforms to be measured have a same shape, which can be described as: $y = F(t) = A \times f(t + \tau) + p = Af(t) + Bf'(t) + p$. Considering that each waveform is fitted by multiple points and there is random noise at each point, the equation can be changed into:

$$\begin{pmatrix} y(t_1) \\ \vdots \\ y(t_n) \end{pmatrix} = \begin{pmatrix} f(t_1) & f'(t_1) & 1 \\ \vdots & \vdots & \vdots \\ f(t_n) & f'(t_n) & 1 \end{pmatrix} \cdot \begin{pmatrix} A \\ B \\ p \end{pmatrix} + \begin{pmatrix} e_1 \\ \vdots \\ e_n \end{pmatrix} \quad (\text{A.1})$$

Rewrite it in matrix form in least square theory:

$$\mathbf{Y} = \mathbf{X}\boldsymbol{\beta} + \mathbf{e} \quad (\text{A.2})$$

$$\mathbf{Y} = \begin{pmatrix} y_1 \\ \vdots \\ y_n \end{pmatrix} = \begin{pmatrix} y(t_1) \\ \vdots \\ y(t_n) \end{pmatrix}, \mathbf{X} = \begin{pmatrix} f(t_1) & f'(t_1) & 1 \\ \vdots & \vdots & \vdots \\ f(t_n) & f'(t_n) & 1 \end{pmatrix}, \boldsymbol{\beta} = \begin{pmatrix} A \\ B \\ p \end{pmatrix}, \mathbf{e} = \begin{pmatrix} e_1 \\ \vdots \\ e_n \end{pmatrix} \quad (\text{A.3})$$

Furthermore, if the variance-covariance matrix of vector \mathbf{e} is a diagonal matrix with a same element as shown in equation (A.4), the estimator $\hat{\boldsymbol{\beta}}$ can be calculated by minimizing the sum of squared errors, as shown in equation (A.5).

$$\begin{aligned}
\mathbf{S} &= \text{Var}(\mathbf{e}) = E[\mathbf{e}\mathbf{e}^T] \\
&= \begin{pmatrix} \text{var}(e_1) & \text{cov}(e_1, e_2) & \cdots & \text{cov}(e_1, e_{n-1}) & \text{cov}(e_1, e_n) \\ \text{cov}(e_2, e_1) & \text{var}(e_2) & \cdots & \text{cov}(e_2, e_{n-1}) & \text{cov}(e_2, e_n) \\ \vdots & \vdots & \vdots & \vdots & \vdots \\ \text{cov}(e_{n-1}, e_1) & \text{cov}(e_{n-1}, e_2) & \cdots & \text{var}(e_{n-1}) & \text{cov}(e_{n-1}, e_n) \\ \text{cov}(e_n, e_1) & \text{cov}(e_n, e_2) & \cdots & \text{cov}(e_n, e_{n-1}) & \text{var}(e_n) \end{pmatrix} \\
&= \begin{pmatrix} \sigma^2 & 0 & \cdots & 0 & 0 \\ 0 & \sigma^2 & \cdots & 0 & 0 \\ \vdots & \vdots & \vdots & \vdots & \vdots \\ 0 & 0 & \cdots & \sigma^2 & 0 \\ 0 & 0 & \cdots & 0 & \sigma^2 \end{pmatrix} = \sigma^2 \mathbf{I}_n
\end{aligned} \tag{A.4}$$

$$\hat{\boldsymbol{\beta}} = \text{argmin} : (\mathbf{Y} - \mathbf{X}\boldsymbol{\beta})^T (\mathbf{Y} - \mathbf{X}\boldsymbol{\beta}) \tag{A.5}$$

Apply the condition that the derivative is zero:

$$\hat{\boldsymbol{\beta}} = (\mathbf{X}^T \mathbf{X})^{-1} \mathbf{X}^T \mathbf{Y} \tag{A.6}$$

If the variance-covariance matrix \mathbf{S} cannot meet the above condition ($\mathbf{S} = \sigma^2 \mathbf{I}_n$), apply the property that variance-covariance matrix \mathbf{S} and its inverse matrix \mathbf{S}^{-1} are both positive definite matrices. There must be a matrix \mathbf{K} which satisfies:

$$\mathbf{S}^{-1} = \mathbf{K}^T \mathbf{K} \tag{A.7}$$

Multiply both sides of equation (A.2):

$$\mathbf{K}\mathbf{Y} = \mathbf{K}\mathbf{X}\boldsymbol{\beta} + \mathbf{K}\mathbf{e} \tag{A.8}$$

Define $\mathbf{Y}_* = \mathbf{K}\mathbf{Y}$, $\mathbf{X}_* = \mathbf{K}\mathbf{X}$, $\mathbf{e}_* = \mathbf{K}\mathbf{e}$ and the above equation is changed into:

$$\mathbf{Y}_* = \mathbf{X}_* \boldsymbol{\beta} + \mathbf{e}_* \tag{A.9}$$

Now, the variance-covariance matrix of the new variable \mathbf{e}_* is:

$$\text{Var}(\mathbf{e}_*) = E[\mathbf{e}_* \mathbf{e}_*^T] = \mathbf{K} E[\mathbf{e} \mathbf{e}^T] \mathbf{K}^T = \mathbf{K} \mathbf{S} \mathbf{K}^T = \mathbf{I}_n \tag{A.10}$$

Hence, the estimator $\hat{\boldsymbol{\beta}}$ can be extracted by these new variables:

$$\hat{\boldsymbol{\beta}} = (\mathbf{X}_*^T \mathbf{X}_*)^{-1} \mathbf{X}_*^T \mathbf{Y}_* = (\mathbf{X}^T \mathbf{K}^T \mathbf{K} \mathbf{X})^{-1} \mathbf{X}^T \mathbf{K}^T \mathbf{K} \mathbf{Y} = (\mathbf{X}^T \mathbf{S}^{-1} \mathbf{X})^{-1} \mathbf{X}^T \mathbf{S}^{-1} \mathbf{Y} \tag{A.11}$$

This equation is the same as equation (2.5) in section 2. Bring the definition of \mathbf{Y} for simplification:

$$\hat{\boldsymbol{\beta}} = (\mathbf{X}^T \mathbf{S}^{-1} \mathbf{X})^{-1} \mathbf{X}^T \mathbf{S}^{-1} (\mathbf{X}\boldsymbol{\beta} + \mathbf{e}) = \boldsymbol{\beta} + (\mathbf{X}^T \mathbf{S}^{-1} \mathbf{X})^{-1} \mathbf{X}^T \mathbf{S}^{-1} \mathbf{e} \tag{A.12}$$

It indicates that the estimator $\hat{\beta}$ is the superposition of the exact value β and an error term. In waveform fitting algorithm, the fitting result is the superposition of the exact value and a noise-induced term. The variance of the fitting result induced by noise is:

$$\begin{aligned}\text{Var}(\hat{\beta}) &= E[(\hat{\beta} - E[\hat{\beta}])(\hat{\beta} - E[\hat{\beta}])^T] \\ &= E[(\mathbf{X}^T \mathbf{S}^{-1} \mathbf{X})^{-1} \mathbf{X}^T \mathbf{S}^{-1} \mathbf{e} (\mathbf{X}^T \mathbf{S}^{-1} \mathbf{X})^{-1} \mathbf{X}^T \mathbf{S}^{-1} \mathbf{e}^T] \\ &= (\mathbf{X}^T \mathbf{S}^{-1} \mathbf{X})^{-1} \mathbf{X}^T \mathbf{S}^{-1} \mathbf{X} \mathbf{X}^T \mathbf{S}^{-1} \mathbf{X} \\ &= (\mathbf{X}^T \mathbf{S}^{-1} \mathbf{X})^{-1}\end{aligned}\quad (\text{A.13})$$

The variance of one specific element caused by noise in $\hat{\beta}$ is:

$$\text{Var}(\hat{\beta}_i) = ((\mathbf{X}^T \mathbf{S}^{-1} \mathbf{X})^{-1})_{ii} \quad (\text{A.14})$$

B Improvement of time resolution with sequence selection optimization

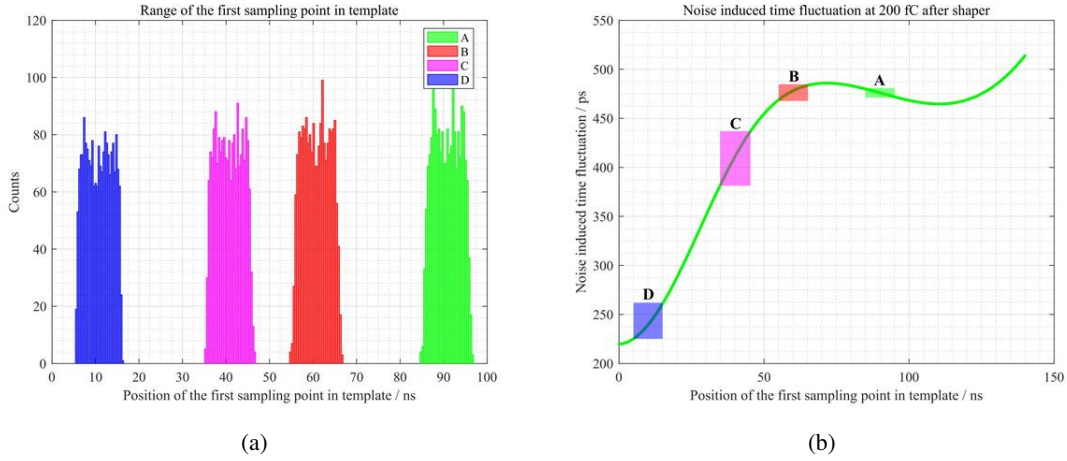


Figure 16. (a): The time distribution of the first point of different sequences after shaper in experiment. (b): The noise induced jitter with different fitting sequences (the horizontal axis represents the time of the first point).

It can be inferred from Figure 12 (b) that choosing a sequence whose first point is close to 0 ns can result in better time resolution. Here are some results based on actual experimental data. Four kinds of sequence selection methods (A, B, C, D) are adopted, in which the first point gradually approaches 0 ns in template from method A to method D. Figure 16 (a) gives the time distribution of the first point in four selections. Figure 16 (b) shows the corresponding calculated timing fluctuations. The actual results by the fitting algorithm are shown in figure 17.

Acknowledgments

The authors thank Hefei Comprehensive National Science Center for their strong support. This work was supported by the Double First-Class university project foundation of USTC.

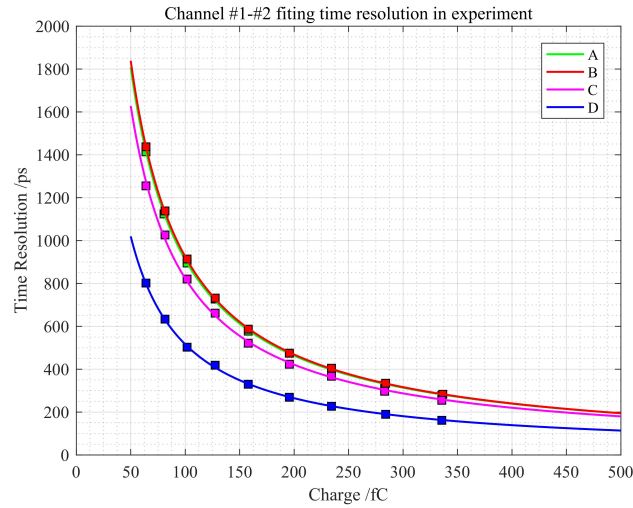


Figure 17. Time resolution calculated by different sequences from the same experimental data after shaper.

References

- [1] Q. Luo, et al., *Progress on Preliminary Conceptual Study of HIEPA, a Super Tau-Charm Factory in China*, in *Proceedings of IPAC 2018*, Vancouver, Canada, 29 April–4 May 2018, pp. 422–424.
- [2] H.P. Peng. *High Intensity Electron Positron Accelerator (HIEPA), Super Tau Charm Facility (STCF) in China*, talk at *Charm2018*, Novosibirsk, Russia, 21–25 May 2018.
- [3] A. Boyarintsev et al., *Study of radiation hardness of pure CsI crystals for Belle-II calorimeter*, [2016 JINST 11 P03013](#).
- [4] F. Yang, L. Zhang and R.-Y. Zhu, *Gamma-Ray Induced Radiation Damage Up to 340 Mrad in Various Scintillation Crystals*, *IEEE Trans. Nucl. Sci.* **63** (2016) 612.
- [5] L. Luo et al., *Design and optimization of the CSA-based readout electronics for STCF ECAL*, [2020 JINST 15 C09002](#).
- [6] M.N. Achasov et al., *SND electromagnetic calorimeter time measurement and its applications*, [2020 JINST 15 C09042](#) [[arXiv:2005.07090](#)].
- [7] BELLE-II collaboration, *Belle II Technical Design Report*, [arXiv:1011.0352](#).